Chemical Mapping of Excitons in Halide Double Perovskites

Raisa-Ioana Biega,[1] Yinan Chen,[2] Marina R. Filip,[2, *] and Linn Leppert[1, †]

[1]*MESA+ Institute for Nanotechnology, University of Twente, 7500 AE Enschede, The Netherlands*

[2]*Department of Physics, University of Oxford, Clarendon Laboratory, Oxford, OX1 3PU, United Kingdom*

(Dated: today)

Halide double perovskites are an emerging class of semiconductors with tremendous chemical and electronic diversity. While their bandstructure features can be understood from frontier-orbital models, chemical intuition for optical excitations remains incomplete. Here, we use *ab initio* many-body perturbation theory within the GW and the Bethe-Salpeter Equation approach to calculate excited-state properties of a representative range of $Cs_2BB'Cl_6$ double perovskites. Our calculations reveal that double perovskites with different combinations of B and B' cations display a broad variety of electronic bandstructures and dielectric properties, and form excitons with binding energies ranging over several orders of magnitude. We correlate these properties with the orbital-induced anisotropy of charge-carrier effective masses and the long-range behavior of the dielectric function, by comparing with the canonical conditions of the Wannier-Mott model. Furthermore, we derive chemically intuitive rules for predicting the nature of excitons in halide double perovskites using electronic structure information obtained from computationally inexpensive DFT calculations.

Halide double perovskites, also known as elpaso-lites, are a class of materials, with the general formula $A_2BB'X_6$, where A is a monovalent cation such as Cs^+, balancing the charge of corner-connected BX_6 and $B'X_6$ metal-halide octahedra. Discovered first in the end of the 19th century in the Rocky Mountains [1], these stable, non-toxic, and earth-abundant semiconductors were initially studied as materials for radiation detection [2, 3]. More recently, halide double perovskites showcased their potential in a range of applications, including photovoltaics [4–13], X-ray detection [14, 15], scintillation [16], white light emission [17, 18], and photocatalysis [19]. This is in large part due to the tremendous chemical and structural diversity of this material class [20–23], that can be achieved by chemical substitution at the B, B', and X sites [24–26].

Understanding optical excitations in halide double perovskites is crucial for designing efficient and stable optoelectronic applications [12, 27–29]. In particular the binding energy of photoexcited electron-hole pairs (excitons) is a useful parameter to determine in studies of charge-carrier transport and recombination, and is thus key for device performance and design. Experimentally, exciton binding energies of halide perovskites have been extracted from optical absorption measurements either by fitting spectra using Elliott's theory [30–32] or by measuring optical absorption spectra under high magnetic fields [33]. These methods generally assume that excitons obey the Wannier-Mott (or hydrogenic) model, which in 3D yields the following expression for the energies of the bound exciton states: $E_n = -\dfrac{\mu}{\varepsilon^2} \cdot \dfrac{1}{n^2}$ (in atomic units), with the binding energy defined as $E_B = -E_1$. The hydrogenic model has been used to understand the photophysics of a wide range of materials, from Pb-based halide perovskites [31, 33–37] to MoS_2 and other layered materials [38–40]. Fundamentally, the hydrogenic model relies on two main assumptions, that electronic bands must be

isotropic and parabolic, and that the dielectric screening of the electron-hole interaction must be uniform (described by the constant relative permittivity) [41]. The degree to which complex heterogeneous semiconductors abide by these tenets determines how accurate the hydrogenic picture is in describing excitons in a material, or (as we denote herein) how '*hydrogenic*' excitons are in a material.

First-principles many-body perturbation theory within the GW approximation [42] and the Bethe-Salpeter Equation [43, 44] (BSE) approach has played a particularly important role in quantitatively predicting the electronic and excited-state structure of halide perovskites. In particular, comparison of GW+BSE calculations with the Wannier-Mott model has demonstrated the hydrogenic nature of excitons in Pb-based halide perovskites [45, 46]. In contrast, we and others recently showed that excitons in the double perovskite family Cs_2AgBX_6 (B=Bi, Sb and X=Br, Cl) [4, 5, 22] exhibit resonant excitons with binding energies between 170 and 450 meV which are strongly localized, with fine-structure features that differ from those computed using the hydrogenic model [47, 48]. We assigned the non-hydrogenic character of excitons in these halide double perovskites to their chemical heterogeneity giving rise to an anisotropic electronic structure and dielectric screening [48].

In Ref. 18, the GW+BSE approach was used to compute the lowest bound excitonic states in $Cs_2AgInCl_6$ which correspond to dipole-forbidden ('dark') optical transitions, readily assigned to the symmetry of the single-particle electronic states at the conduction and valence band edges [49]. The lowest of these *dark* excitons was reported to have a binding energy of 250 meV, but its hydrogenic nature was not investigated. However, Ref. 50 used the Wannier-Mott model to calculate the exciton binding energy of $Cs_2AgInCl_6$ and found a value of 215 meV, similar to the first-principles result reported in

Ref. 18. For other halide double perovskites with different combinations of metal sites, optoelectronic properties and exciton binding energies were shown to vary significantly too [51–53]. The picture that emerges from these reports suggests a rich landscape of excitons in halide double perovskites and calls for a systematic mapping of this landscape using first-principles calculations.

In this letter, we use the GW+BSE approach to develop a holistic understanding of how the electronic structure of the alternating B- and B′-site cations influences the nature of excitons in halide double perovskites. By studying a representative set of halide double perovskites $Cs_2BB'Cl_6$, we show that exciton binding energies can be tuned by several orders of magnitude through chemical substitution at the B and B′ sites. Furthermore, we demonstrate that direct band gap halide double perovskites with isotropic, parabolic band edges and small local field effects in their dielectric screening, feature delocalized hydrogenic excitons similar to their Pb-based single perovskite congeners. However, the absorption spectra of these materials depend considerably on the symmetry of the band edges, and can deviate significantly from expectations prescribed by canonical models. Among the heterogeneous double perovskites we study systematically, we find that some (but not all) exhibit an exciton fine structure which is well described by the hydrogenic model. However, the extent to which excitons present as non-hydrogenic depends strongly on the electronic structure of the alternating B and B′ metals.

Recently, Ref. 46 showed that the fully inorganic Pb-based halide perovskites feature highly delocalized hydrogenic excitons. Here we use the cubic phase of $CsPbCl_3$ (referred to as **Pb** in the following) as a prototypical case of a direct band gap single perovskite, which we compare to seven representative cubic double perovskites $A_2BB'X_6$ with $A = Cs^+$ and $X = Cl^-$ (denoted by **B/B′** in the following). Our goal is to identify how the electronic structure of the B- and B′-site cations determines the hydrogenic nature of excitons in halide double perovskites. To this end, we explore double perovskites featuring metals from across the periodic table (Figure 1(a)): **In/Bi**, which is isoelectronic to **Pb**; **Ag/In** and **Na/In** which feature a direct band gap, and large band dispersion, but a distinctly different band edge orbital character than **In/Bi**; and **Ag/Bi**, **Ag/Sb**, **Na/Bi** and **K/Bi** with an indirect band gap and low-dispersion band edges. With the exception of **In/Bi**, these double perovskites have all been synthesized and experimentally characterized [4, 5, 18, 54–60]. The Na- and K-based compounds have experimentally been studied as favorable host structures for luminescent centers such as Mn^{2+} and Sb^{3+} [58–60]. However, to the best of our knowledge, we are the first to perform state-of-the-art GW+BSE calculations for these materials and report their exciton binding energies.

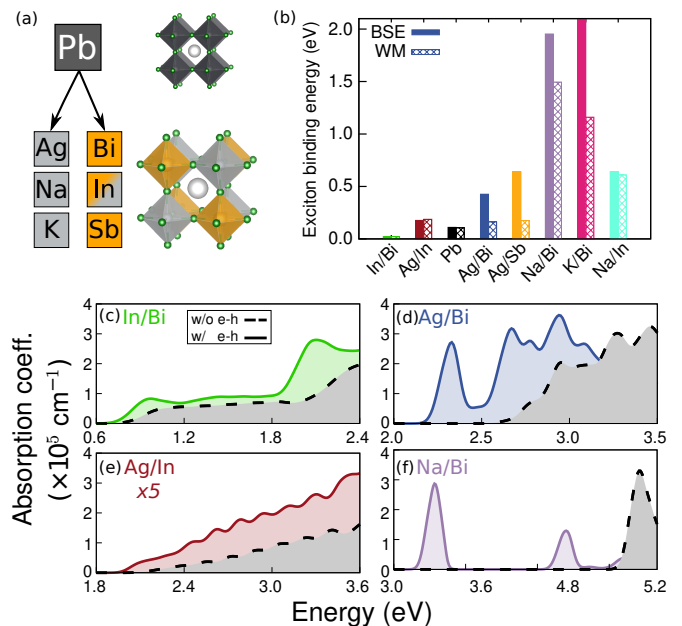We start by calculating the quasiparticle (QP) band

FIG. 1. (a) Overview of materials studied. In the cubic structures of single and double perovskites, X sites (Cl^-) are green, A sites (Cs^+) are white, dark gray corresponds to Pb, light-grey to the B and orange to the B′ site. (b) Exciton binding energy computed from first principles (solid bars), and estimated based on the Wannier-Mott fine structure, as described in the text (patterned bars). Materials appear in order of their QP band gap with the lowest band-gap material on the left. Linear optical absorption spectra, calculated using the independent-particle approximation (black dashed line), and the G_0W_0+BSE approach (solid colored line) for (c) **In/Bi**, (d) **Ag/Bi**, (e) **Ag/In** and (f) **Na/Bi**.

structure, absorption spectra and exciton binding energies of all eight materials using the GW+BSE approach as implemented in the BERKELEYGW code [61, 62] (see the Supporting Information (SI) and Figures S1 – S3 for further computational details and convergence studies). Figure 1(b) shows the exciton binding energy from first-principles calculations (BSE) and estimated according to the Wannier-Mott fine structure (WM). BSE exciton binding energies (E_{BSE}) are calculated as the difference between the energy of the first excited state and the direct QP band gap. Here, and unless otherwise noted, we quantify agreement with the Wannier-Mott model by computing the energy difference $E^{1s-2s} = \frac{4}{3} \cdot (E_{2s} - E_{1s})$, i.e., from the difference between the G_0W_0+BSE excitation energies of the 1s (E_{1s}) and 2s (E_{2s}) states, respectively (see SI and Figure S4 for exciton fine structures and assignment of the 1s and 2s states). Table I reports the QP band gaps and exciton binding energies of all eight materials.

Figure 1(b) and Table I allow for several observations: First, our selected double perovskites span a wide range of QP band gaps between ∼1 and 5 eV, which

are inversely proportional to their dielectric constants ε_∞ (see Figure S5). Consequently, the exciton binding energies of these compounds differ by several orders of magnitude. Depending on B and B$'$ site occupation, E_{BSE} ranges from 16 meV (**In/Bi**) to $\sim$2 eV (**K/Bi**). However, as shown in Figure S6, E_{BSE} does not scale linearly with $1/\varepsilon_\infty^2$, suggesting that the Wannier-Mott model performs poorly for a subset of double perovskites. Indeed, the first-principles exciton binding energies of **Ag/Bi**, **Ag/Sb**, **Na/Bi**, and **K/Bi** deviate by several hundred meV from the Wannier-Mott fine structure. In contrast, and despite their seemingly similar degree of chemical heterogeneity, **Ag/In**, **In/Bi**, and **Na/In** feature hydrogenic excitons, similar to the single perovskite **Pb** [46]. We therefore separate the studied double perovskites in two groups: materials with *hydrogenic* (**Pb**, **Bi/In**, **Ag/In**, **Na/In**) and materials with *non-hydrogenic* (**Ag/Bi**, **Ag/Sb**, **Na/Bi**, **K/Bi**) exciton fine structures. Notably, we find that $\Delta_{\mathrm{WM}} = E_{\mathrm{BSE}} - E^{1s-2s}$, does not necessarily increase with increasing exciton binding energy. In other words, the magnitude of the exciton binding energy does not necessarily explain the observed non-hydrogenic fine structure. For example, **Na/In** features a hydrogenic 1s exciton with a very high binding energy of $\sim$600 meV.

Not only the exciton binding energies, but also the absorption spectra of these eight materials differ significantly. In Figure 1(c), (e) and (d), (f) we show the calculated linear optical absorption spectra of representative double perovskites with *hydrogenic* and *non-hydrogenic* excitons, respectively. The absorption spectra of all other materials can be found in Figure S7 of the SI. Inclusion of electron-hole interactions red-shifts the absorption spectra as compared to the independent-particle picture. The absorption spectrum of **In/Bi** exhibits a distinct excitonic feature at the absorption onset, which appears suppressed in comparison to the excitonic feature of **Pb**. This is due to the significantly lower band gap and exciton binding energy of this material, and the arbitrary broadening of 50 meV chosen throughout. In agreement with previous results [18], we observe that **Ag/In** and **Na/In** have a weak absorption onset and do not exhibit a signature excitonic peak. The absorption coefficient is also one order of magnitude lower than that of the other materials. This is in line with the dipole-forbidden transitions between the valence and conduction band edges [49] of these materials. In contrast, all four materials with *non-hydrogenic* excitons feature one or several distinct excitonic peaks at the onset of absorption.

In all materials studied, the lowest excited state is dipole forbidden. For **Ag/In** and **Na/In**, in which SOC does not affect the valence and conduction band edges, this is a result of the angular-momentum symmetry of the atomic orbitals contributing to the valence and conduction band edges [49]. For the other six materials, the CBM is originating from Bi, Sb or Pb p orbitals, and the

inclusion of SOC leads to a splitting of the four degenerate excited states arising from VBM to CBM transitions into a lowest-energy dark and three (nearly) degenerate bright states with oscillator strengths consistent with selection rules [63–65].

Having established these subsets of materials with *hydrogenic* and *non-hydrogenic* excitons, we continue by probing to which degree the main assumptions of the Wannier-Mott model – isotropic, parabolic band edges and a uniform, isotropic dielectric constant – are fulfilled for these materials. We start by assessing the dispersion of their conduction and valence band edges by calculating the effective electron and hole masses (a complete overview of DFT and G_0W_0 band gaps and bandstructures can be found in Table S3 and Figures S8 and S9). The effective electron and hole masses along the principal axis of the effective mass tensor of all materials can be identified as longitudinal and transverse effective masses (Table II), similar to other fcc semiconductors such as Si and GaAs [66]. We describe our procedure for calculating and defining longitudinal and transverse effective masses in the SI and show the valence and conduction band edges along those directions in Figure 2(a) and (b), for **In/Bi** and **Ag/Bi**, representative for double perovskites with *hydrogenic* and *non-hydrogenic* excitons, respectively. Inspection of the energy band dispersion around the high symmetry point of the lowest-energy direct transition – Γ [0, 0, 0] for **In/Bi** and X [0, 1, 0]$2\pi/a$ for **Ag/Bi** – demonstrates that the band edges of **In/Bi** are isotropic around Γ, while those of **Ag/Bi** are highly anisotropic around X, featuring different curvatures in the longitudinal and transverse directions.
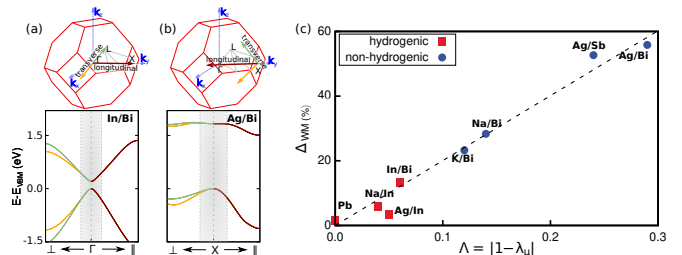

FIG. 2. Graphical representation of the Brillouin zone and the DFT-PBE+SOC conduction and valence bands of (a) **In/Bi** and (b) **Ag/Bi** along the transversal (X/$\Gamma \to \perp$) and longitudinal (X/$\Gamma \to \parallel$) directions. The shaded area corresponds to the **k**-interval used to compute the effective masses. (c) Variation of the relative deviation Δ_{WM} of the Wannier-Mott fine structure with respect to the first-principles (BSE) result as a function of the effective mass anisotropy $\Lambda = |1 - \lambda_\mu|$.

Further analysis reveals that the effective mass anisotropy factor $\lambda_\mu = \left(\dfrac{\mu_\perp}{\mu_\parallel}\right)^{1/3}$ is close to 1 for the double perovskites with *hydrogenic* excitons and exactly 1 for **Pb**. In Figure 2(c) we show Δ_{WM} as a function of the quantity $\Lambda = |1 - \lambda_\mu|$, where $\Lambda = 0$ corresponds

hydrogenic

System B/B′	QP direct gap (eV) $E_{\mathrm{gap}}^{G_0W_0}$	Static dielectric constant ε_∞	Exciton binding energy (eV) BSE $E_{\mathrm{dark}}^{\mathrm{BSE}}$	$E_{\mathrm{bright}}^{\mathrm{BSE}}$	Wannier-Mott E^{1s-2s}
Pb	2.25	3.67	0.105	0.104	0.103
In/Bi	0.90	5.63	0.021	0.020	0.018
Ag/In	2.09	3.75	0.176	0.049	0.170
Na/In	5.52	2.78	0.642	0.135	0.605

non-hydrogenic

System B/B′	QP direct gap (eV) $E_{\mathrm{gap}}^{G_0W_0}$	Static dielectric constant ε_∞	Exciton binding energy (eV) BSE $E_{\mathrm{dark}}^{\mathrm{BSE}}$	$E_{\mathrm{bright}}^{\mathrm{BSE}}$	Wannier-Mott E^{1s-2s}
Ag/Bi	2.64	4.49	0.426	0.329	0.206
Ag/Sb	3.20	4.63	0.639	0.549	0.302
Na/Bi	4.93	3.09	1.953	1.611	0.553
K/Bi	4.99	2.73	2.091	1.725	0.487

TABLE I. G_0W_0@PBE lowest direct band gap, static dielectric constant as computed within the random phase approximation, E^{BSE} of the first dark and first bright excited state and E^{1s-2s}.

to a fully isotropic material (e.g., **Pb**). This analysis shows that the relative deviation from the Wannier-Mott model scales almost linearly with the degree of anisotropy. The materials with *hydrogenic* excitons (red squares) are mostly isotropic and feature a deviation of no more than 14 % from the Wannier-Mott model. In contrast, the double perovskites with *non-hydrogenic* excitons (blue dots) show a significantly higher degree of anisotropy and a large deviation from the Wannier-Mott model. We note that accounting for the effective mass anisotropy in the Wannier-Mott model following Ref. 67 reduces Δ_{WM} by 14% to 30% for the materials with non-hydrogenic excitons, but does not fully account for the observed deviations (see Table S4).

Next, we probe the uniformity and isotropy of the dielectric screening, i.e., local field effects of the dielectric function, in two ways. First, we compute linear absorption spectra (i.e. the imaginary part of the dielectric function), by modifying the real part of the dielectric function such that $\mathrm{Re}[\epsilon(\mathbf{r},\mathbf{r}';\omega)] = \varepsilon_\infty$. We find that optical absorption spectra and exciton binding energies change significantly only for those perovskites in which excitons do not display hydrogenic behavior (see Figure S7). Second, we analyze the spatial dependence of the head, i.e., the $\mathbf{G} = \mathbf{G}' = 0$ component, of the dielectric function. Figure 3(a) and Figure S10 show that we can fit this spatial dependence with the model dielectric function,

$$\mathrm{Re}[\epsilon(q,0)] = 1 + \left[(\varepsilon_\infty - 1)^{-1} + \alpha\left(\frac{q}{q_{TF}}\right)^2\right]^{-1},$$ with α

and the Thomas-Fermi wave vector, q_{TF} as fitting parameters tabulated in Table S5 and ε_∞ the RPA dielectric constant [68].

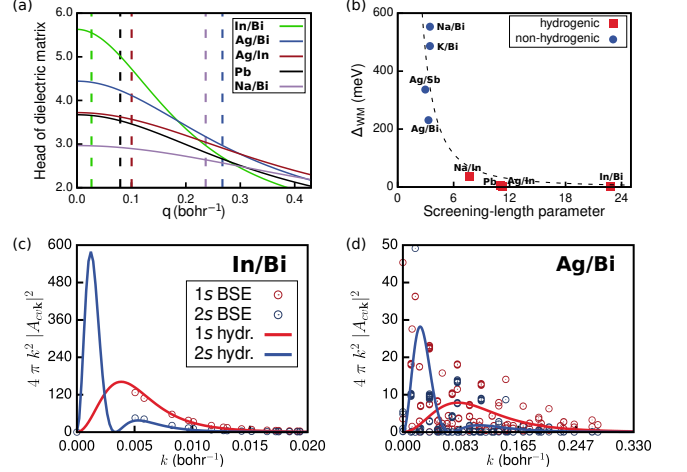We then compare the length scale of dielectric screen-

FIG. 3. (a) Model dielectric function (as described in the text) in reciprocal space for **In/Bi** (green), **Ag/Bi** (blue), **Ag/In** (red), **Pb** (black), and **Na/Bi** (purple). The corresponding colored dashed line shows the exciton extent in **k**-space (k_x) as defined in the text. (b) Absolute variation of $\Delta_{\mathrm{hydr.}}$ as a function of the screening-length parameter $l = \frac{q_{\mathrm{TF}}}{k_\mathrm{x}}$. Exciton radial probability density in reciprocal space as computed from G_0W_0+BSE (empty disks) and as predicted by the Wannier-Mott model (solid lines) for $1s$ (red) and $2s$ (blue) states for (c) **In/Bi** and (d) **Ag/Bi**.

ing – quantified by q_{TF} – with the length scale of the excitonic wave function of the first excited state k_x in reciprocal space, by calculating the screening length parameter $l = \frac{q_{TF}}{k_x}$ (Table II). For this, we define k_x such that it includes 99 % of the exciton probability density of the first excited state. Figure 3(b) shows that Δ_{WM} decreases as $1/l^2$. Perovskites with *hydrogenic* excitons

feature large screening-length parameters ($l \geq 11$), corresponding to excitons highly localized in reciprocal space, for which the dielectric screening can be assumed to be uniform and constant. In contrast, for the subset of materials with *non-hydrogenic* excitons, the variation of the dielectric constant is significant on the length scale of their excitons, which are strongly delocalized in reciprocal space. Deviations from the Wannier-Mott model in these materials are also apparent by comparing the excitonic wave functions computed with G_0W_0+BSE with the radial probability density of hydrogenic $1s$ and $2s$ excitonic wavefunctions, shown in Figure 3(c) and (d) for **In/Bi** and **Ag/Bi**, respectively (see Figure S11 for the other materials).

Finally, we return to our goal of mapping the character of excitons in halide double perovskites to the band edge electronic structure obtained from computationally inexpensive DFT calculations or derived from chemical intuition (instead of a full solution of the BSE). We note in passing that the effective mass anisotropy can be approximated using DFT effective masses (see Table S3). Chemical intuition for the reciprocal space location, parity, and dispersion of the VBM and CBM can be obtained based on knowledge of the metal-orbital character of the band edges of halide perovskites, as shown in Ref. 69 using linear combinations of atomic orbitals and symmetry arguments. Table III shows the calculated B-site orbital character and high-symmetry **k**-point of the VBM and CBM of all eight perovskites, in agreement with previous predictions [69], and lists the B-site orbital character at the lowest direct transition from which excitons are derived. We observe that in all materials with *non-hydrogenic* excitons, the B-site orbital contributions to the band edges lead to an indirect band gap. The lowest direct transition in these materials occurs at the Brillouin zone boundaries (X in **Ag/Bi** and **Ag/Sb**, and L in **K/Bi** and **Na/Bi**). Furthermore, in all those materials the conduction band edge at the lowest direct transition is relatively flat along the transverse directions which is a consequence of small B and B' site orbital overlap. In **Ag/Bi** and **Ag/Sb**, there is no Ag s character at the X points due to orbital symmetry. In **Na/Bi** and **K/Bi**, Na s and K s contribute to the conduction band edge at L but their overlap with the neighboring Bi p orbitals is small leading to high effective masses in the transverse direction.

Materials with *hydrogenic* excitons have in common that there is a symmetry match of the B- and B'- site orbitals leading to a direct band gap at Γ with isotropic effective masses in valence and conduction band. Note that a direct gap can also arise in a double perovskite in which only one or none of the metal sites contributes to the band edges [69]. In **Na/In**, the valence band edge is rather flat because it does not feature metal-site orbital contributions. However, the conduction band minimum – with contributions from Na s and In s – is at Γ, disperse

and isotropic.

Our predictions can also be extended to double perovskites with one B-site only, such as the vacancy-ordered perovskites with chemical formula Cs_2BX_6. GW+BSE calculations by Cucco *et al.* for Cs_2TeBr_6 and Kavanagh *et al.* for Cs_2TiX_6 (X=I, Br, Cl) indicate highly localized excitons ill-described by the Wannier-Mott model for these materials [70, 71]. Cs_2SnX_6, on the other hand, features delocalized *hydrogenic* excitons, as reported in both Ref. 70 and 71. Using Cs_2TeBr_6, Cs_2TiBr_6, and Cs_2SnBr_6 as examples, we calculated the orbital character of the band edges and effective mass anisotropy using DFT-PBE+SOC (see Table S6). The band structure of Cs_2TeBr_6 is reminiscent of that of **Ag/Bi** and **Ag/Sb** with Te $6s$ and $6p$ contributions leading to an indirect band gap. The lowest direct transition is at L, where the conduction band is derived from Te p orbitals alone and therefore anisotropic. Cs_2TiBr_6 is another indirect-gap semiconductor. Its relatively flat and highly anisotropic conduction band is derived from localized Ti d states and features weak Ti d–X p mixing. Cs_2SnBr_6 on the other hand is comparable to **Na/In** with a direct band gap at Γ and an isotropic conduction band derived from Sn s orbitals (Table III).

In conclusion, we performed a detailed first-principles study of the optoelectronic properties of a set of representative $Cs_2BB'Cl_6$ double perovskites and compared them with those of the single perovskite $CsPbCl_3$ with its known *hydrogenic* exciton series. Chemical substitution at the B and B' metal sites allows for the realization of a wide variety of electronic structure properties with significant orbital-dependent effects on the anisotropy of charge carrier effective masses and dielectric screening. Furthermore, the band gaps of these perovskites also vary by several eV leading to profound differences in the screening of excited electron-hole pairs. Our calculations show that the chemical heterogeneity inherently present in double perovskites due to their alternating B and B' site-centered metal-halide octahedra only leads to *non-hydrogenic* excitons for B and B' site combinations that result in indirect band gaps and large effective mass anisotropies at the band edges. In these double perovskites, excitons are strongly delocalized in reciprocal space and thus experience the full spatial variation of the dielectric screening. On the other hand, excitons in perovskites with isotropic and disperse band edges and delocalized valence and conduction band states are more localized in reciprocal space. We show that our understanding of excitons in halide double perovskites is more general and can be extended to vacancy-ordered perovskites with a single B-site. The nature of excitons in double perovskites can thus be predicted based on electronic structure properties that can be extracted from computationally efficient DFT calculations. With these insights our state-of-the-art GW+BSE calculations can provide a starting point for the development of tight-

hydrogenic

System B/B′	Reduced mass and anisotropy		Screening-length parameter	Deviation from Wannier-Mott	
	μ	λ_μ	$l = \frac{q_{\text{TF}}}{k_{\text{x}}}$	$\Delta_{\text{hydr.}}$ (%)	$\Delta_{\text{hydr.}}$ (meV)
Pb	0.105	1.00	11.22	1.48	1.54
In/Bi	0.052	0.94	22.87	13.43	2.77
Ag/In	0.191	1.05	11.04	3.54	6.23
Na/In	0.345	0.96	7.71	5.73	36.74

non-hydrogenic

System B/B′	Reduced mass and anisotropy		Screening-length parameter	Deviation from Wannier-Mott	
	μ	λ_μ	$l = \frac{q_{\text{TF}}}{k_{\text{x}}}$	$\Delta_{\text{hydr.}}$ (%)	$\Delta_{\text{hydr.}}$ (meV)
Ag/Bi	0.241	1.29	3.30	55.82	230.83
Ag/Sb	0.250	1.23	2.96	52.66	336.38
Na/Bi	0.257	0.86	3.46	28.34	553.39
K/Bi	0.636	0.88	3.46	23.27	486.63

TABLE II. G_0W_0@PBE reduced effective mass μ (in units of the electron rest mass m_0), anisotropy factor λ_μ, static dielectric constant (within the random phase approximation), screening-length parameter and relative and absolute deviation of the Wannier-Mott exciton binding energy with respect to the first-principles (BSE) result.

binding models for excitons, aid in the interpretation of experiments, and inspire further study of excited state properties of this complex quarternary family of materials.

SUPPORTING INFORMATION

Methodological and computational details (including convergence plots), DFT and QP electronic band structures, absorption spectra, exciton diagrams, radial probability density, and variation of dielectric constant in reciprocal space.

* marina.filip@physics.ox.ac.uk
† l.leppert@utwente.nl

[1] C. W. Cross and W. F. Hillebrand, On minerals of the cryolite group recently found in Colorado, Am. J. Sci. **s3-26**, 271 (1883).

[2] H. G. Brittain and G. Meyer, Cryogenic luminescence studies of Eu^{3+} in $LiEuCl_4$, J. Solid State Chem. **59**, 183 (1985).

[3] T. Pawlik and J.-M. Spaeth, Investigation of radiation-induced defects in Cs_2NaYF_6, Phys. Status Solidi B **203**, 43 (1997).

[4] E. T. McClure, M. R. Ball, W. Windl, and P. M. Woodward, Cs2AgBiX6 (X = Br, Cl) — New visible light absorbing, lead-free halide perovskite semiconductors, Chem. Mater **6**, 1348 (2016).

[5] A. H. Slavney, T. Hu, A. M. Lindenberg, and H. I. Karunadasa, A Bismuth-Halide Double Perovskite with Long Carrier Recombination Lifetime for Photovoltaic Applications, J. Am. Chem. Soc. **138**, 2138 (2016).

[6] E. Greul, M. L. Petrus, A. Binek, P. Docampo, and T. Bein, Highly stable, phase pure $Cs_2AgBiBr_6$ double perovskite thin films for optoelectronic applications, J. Mater. Chem. A **5**, 19972 (2017).

[7] X.-G. Zhao, J.-H. Yang, Y. Fu, D. Yang, Q. Xu, L. Yu, S.-H. Wei, and L. Zhang, Design of lead-free inorganic halide perovskites for solar cells via cation-transmutation, J. Am. Chem. Soc. **139**, 2630 (2017).

[8] G. Volonakis, A. A. Haghighirad, R. L. Milot, W. H. Sio, M. R. Filip, B. Wenger, M. B. Johnston, L. M. Herz, H. J. Snaith, and F. Giustino, $Cs_2InAgCl_6$: A New Lead-free Halide Double Perovskite with Direct Band Gap, J. Phys. Chem. Lett. **8**, 772 (2017).

[9] L. Debbichi, S. Lee, H. Cho, A. M. Rappe, K.-H. Hong, M. S. Jang, and H. Kim, Mixed Valence Perovskite Cs2Au2I6 : A Potential Material for Thin-Film Pb-Free Photovoltaic Cells with Ultrahigh Efficiency, Adv. Mater. **30**, 1707001 (2018).

[10] A. Fakharuddin, U. Shabbir, W. Qiu, T. Iqbal, M. Sultan, P. Heremans, and L. Schmidt-Mende, Inorganic and layered perovskites for optoelectronic devices, Adv. Mater. **31**, 1807095 (2019).

[11] X. Yang, Y. Chen, P. Liu, H. Xiang, W. Wang, R. Ran, W. Zhou, and Z. Shao, Simultaneous Power Conversion Efficiency and Stability Enhancement of $Cs_2AgBiBr_6$ Lead-Free Inorganic Perovskite Solar Cell

System	Band gap			Lowest direct trans.			Anisotropy		Exciton
	valence	conduction	**k**-point	valence	conduction	**k**-point	pred.	calc.	
Ag/Bi	Ag $4d_{z^2}$ Bi $6s$	Ag $5s$ Bi $6p$	Indirect X→L	Ag $4d_{z^2}$ Bi $6s$	*Null* Bi $6p$	X	high Λ	high Λ	non-hydr.
Ag/Sb	Ag $4d_{z^2}$ Sb $5s$	Ag $5s$ Sb $5p$	Indirect X→L	Ag $4d_{z^2}$ Sb $5s$	*Null* Sb $5p$	X	high Λ	high Λ	non-hydr.
K/Bi	*Null* Bi $6s$	K $4s$ Bi $6p$	Indirect L→ Γ Direct Γ	*Null* Bi $6s$	K $4s$ Bi $6p$	L	high Λ	high Λ	non-hydr.
Na/Bi	*Null* Bi $6s$	Bi $6p$ Na $3s$	Indirect X→ Γ	*Null* Bi $6s$	Na $3s$ Bi $6p$	L	high Λ	high Λ	non-hydr.
Ag/In	Ag $4d_{z^2/x^2-y^2}$ *Null*	Ag $5s$ In $5s$	Direct Γ	Ag $4d_{z^2/x^2-y^2}$ *Null*	Ag $5s$ In $5s$	Γ	low Λ	low Λ	hydr.
Na/In	*Null* *Null*	Na $3s$ In $5s$	Direct Γ	*Null* *Null*	Na $3s$ In $5s$	Γ	low Λ	low Λ	hydr.
In/Bi	In $5s$ Bi $6s$	In $5p$ Bi $6p$	Direct Γ	In $5s$ Bi $6s$	In $5p$ Bi $6p$	Γ	low Λ	low Λ	hydr.
Pb	Pb $6s$	Pb $6p$	Direct R	Pb $6s$	Pb $6p$	R	no Λ	no Λ	hydr.
Cs$_2$TeBr$_6$	Te $6s$	Te $6p$	Indirect X→L	Te $6s$	Te $6p$	L	high Λ	high Λ	non-hydr.
Cs$_2$TiBr$_6$	*Null*	Ti $3d_{xy}$	Indirect Γ →X	*Null*	Ti $3d_{xy}$	Γ	high Λ	high Λ	non-hydr.
Cs$_2$SnBr$_6$	*Null*	Sn $5s$	Direct Γ	*Null*	Sn $5s$	Γ	low Λ	low Λ	hydr.

TABLE III. Metal-orbital character of the band edges, nature of the band gap, effective mass anisotropy and nature of the exciton for the analysed materials and vacancy-ordered perovskites Cs$_2$TeBr$_6$, Cs$_2$TiBr$_6$, and Cs$_2$SnBr$_6$. Contributions from halogen atoms are omitted for clarity.

through Adopting a Multifunctional Dye Interlayer, Adv. Func. Mater. **30**, 2001557 (2020).

[12] G. Longo, S. Mahesh, L. R. V. Buizza, A. D. Wright, A. J. Ramadan, M. Abdi-Jalebi, P. K. Nayak, L. M. Herz, and H. J. Snaith, Understanding the Performance-Limiting Factors of Cs$_2$AgBiBr$_6$ Double-Perovskite Solar Cells, ACS Energy Lett. **5**, 2200 (2020).

[13] M. T. Sirtl, R. Hooijer, M. Armer, F. G. Ebadi, M. Mohammadi, C. Maheu, A. Weis, B. T. van Gorkom, S. Häringer, R. A. J. Janssen, T. Mayer, V. Dyakonov, W. Tress, and T. Bein, 2D/3D Hybrid Cs$_2$AgBiBr$_6$ Double Perovskite Solar Cells: Improved Energy Level Alignment for Higher Contact-Selectivity and Large Open Circuit Voltage, Adv. Energy Mater. **12**, 2103215 (2022).

[14] W. Pan, H. Wu, J. Luo, Z. Deng, C. Ge, C. Chen, X. Jiang, W.-J. Yin, G. Niu, L. Zhu, L. Yin, Y. Zhou, Q. Xie, X. Ke, M. Sui, and J. Tang, Cs$_2$AgBiBr$_6$ single-crystal X-ray detectors with a low detection limit, Nat. Photon **11**, 726 (2017).

[15] J. A. Steele, W. Pan, C. Martin, M. Keshavarz, E. Debroye, H. Yuan, S. Banerjee, E. Fron, D. Jonckheere, C. W. Kim, W. Baekelant, G. Niu, J. Tang, J. Vanacken, M. Van der Auweraer, J. Hofkens, and M. B. J. Roeffaers, Photophysical Pathways in Highly Sensitive Cs$_2$AgBiBr$_6$ Double-Perovskite Single-Crystal X-Ray Detectors, Adv. Mater. **30**, 1804450 (2018).

[16] K. Biswas and M. H. Du, Energy transport and scintillation of cerium-doped elpasolite Cs$_2$LiYCl$_6$: Hybrid density functional calculations, Phys. Rev. B **86**, 1 (2012).

[17] B. Yang, X. Mao, F. Hong, W. Meng, Y. Tang, X. Xia, S. Yang, W. Deng, and K. Han, Lead-Free Direct Band Gap Double-Perovskite Nanocrystals with Bright Dual-Color Emission, J. Am. Chem. Soc. **140**, 17001 (2018).

[18] J. Luo, X. Wang, S. Li, J. Liu, Y. Guo, G. Niu, L. Yao, Y. Fu, L. Gao, Q. Dong, C. Zhao, M. Leng, F. Ma, W. Liang, L. Wang, S. Jin, J. Han, L. Zhang, J. Etheridge, J. Wang, Y. Yan, E. H. Sargent, and J. Tang, Efficient and stable emission of warm-white light from lead-free halide double perovskites, Nature **563**, 541 (2018).

[19] L. A. Muscarella and E. M. Hutter, Halide Double-Perovskite Semiconductors beyond Photovoltaics, ACS Energy Lett. **7**, 2128 (2022).

[20] R. E. Brandt, V. Stevanovi, D. S. Ginley, and T. Buonassisi, Identifying defect-tolerant semiconductors with high minority carrier lifetimes : Beyond hybrid lead halide perovskites, MRS Commun. **5**, 265 (2015).

[21] F. A. Faber, A. Lindmaa, O. A. Von Lilienfeld, and R. Armiento, Machine Learning Energies of 2 Million Elpasolite (ABC$_2$D$_6$) Crystals, Phys. Rev. Lett. **117**, 135502 (2016).

[22] G. Volonakis, M. R. Filip, A. A. Haghighirad, N. Sakai, B. Wenger, H. J. Snaith, and F. Giustino, Lead-Free Halide Double Perovskites via Heterovalent Substitution of Noble Metals, J. Phys. Chem. Lett. **7**, 1254 (2016).

[23] M. R. Filip and F. Giustino, The geometric blueprint of perovskites, Proc. Nat. Acad. Sci. **115**, 5397 (2018).

[24] Z. Deng, F. Wei, S. Sun, G. Kieslich, A. K. Cheetham, and P. D. Bristowe, Exploring the properties of lead-free hybrid double perovskites using a combined computational-experimental approach, J. of Mater. Chem. A **4**, 12025 (2016), arXiv:1606.02916.

[25] A. Jain, O. Voznyy, and E. H. Sargent, High-Throughput Screening of Lead-Free Perovskite-like Materials for Optoelectronic Applications, J. Phys. Chem. C **121**, 7183 (2017).

[26] N. R. Wolf, B. A. Connor, A. H. Slavney, and H. I. Karunadasa, Doubling the Stakes: The Promise of Halide Double Perovskites, Ang. Chem. Int. Ed. **60**, 16264 (2021).

[27] L. Schade, A. D. Wright, R. D. Johnson, M. Dollmann, B. Wenger, P. K. Nayak, D. Prabhakaran, L. M. Herz, R. Nicholas, H. J. Snaith, and P. G. Radaelli, Structural and Optical Properties of $Cs_2AgBiBr_6$ Double Perovskite, ACS Energy Lett. **4**, 299 (2019).

[28] M. Roknuzzaman, C. Zhang, K. K. Ostrikov, A. Du, H. Wang, L. Wang, and T. Tesfamichael, Electronic and optical properties of lead-free hybrid double perovskites for photovoltaic and optoelectronic applications, Scientific Reports **9**, 718 (2019).

[29] A. Dey, A. F. Richter, T. Debnath, L. Polavarapu, and J. Feldmann, Transfer of Direct to Indirect Bound Excitons by Electron Intervalley Scattering in Cs2AgBiBr6 Double Perovskite Nanocrystals, ACS Nano **14**, 5855 (2020).

[30] R. J. Elliott, Intensity of optical absorption by excitons, Phys. Rev. **108**, 1384 (1957).

[31] C. L. Davies, M. R. Filip, J. B. Patel, T. W. Crothers, C. Verdi, A. D. Wright, R. L. Milot, F. Giustino, M. B. Johnston, and L. M. Herz, Bimolecular recombination in methylammonium lead triiodide perovskite is an inverse absorption process, Nat. Comm **9**, 293 (2018).

[32] A. D. Wright, L. R. Buizza, K. J. Savill, G. Longo, H. J. Snaith, M. B. Johnston, and L. M. Herz, Ultrafast Excited-State Localization in $Cs_2AgBiBr_6$ Double Perovskite, J. Phys. Chem. Lett. **12**, 3352 (2021).

[33] A. Miyata, A. Mitioglu, P. Plochocka, O. Portugall, J. T.-W. Wang, S. D. Stranks, H. J. Snaith, and R. J. Nicholas, Direct measurement of the exciton binding energy and effective masses for charge carriers in organic–inorganic tri-halide perovskites, Nat. Phys. **11**, 582 (2015).

[34] M. Hirasawa, T. Ishihara, T. Goto, K. Uchida, and N. Miura, Magnetoabsorption of the lowest exciton in perovskite-type compound $(CH_3NH_3)PbI_3$, Phys. B Condens. Matter **201**, 427 (1994).

[35] K. Tanaka, T. Takahashi, T. Ban, T. Kondo, K. Uchida, and N. Miura, Comparative study on the excitons in lead-halide-based perovskite-type crystals $CH_3NH_3PbBr_3$ $CH_3NH_3PbI_3$, Solid State Commun. **127**, 619 (2003).

[36] K. Galkowski, A. Mitioglu, A. Miyata, P. Plochocka, O. Portugall, G. E. Eperon, J. T.-W. Wang, T. Stergiopoulos, S. D. Stranks, H. Snaith, and R. J. Nicholas, Determination of the exciton binding energy and effective masses for methylammonium and formamidinium lead tri-halide perovskite semiconductors, Energy Env. Sci **9**, 962 (2016).

[37] S. Wang, M. Dyksik, C. Lampe, M. Gramlich, D. K. Maude, M. Baranowski, A. S. Urban, P. Plochocka, and A. Surrente, Thickness-Dependent Dark-Bright Exciton Splitting and Phonon Bottleneck in $CsPbBr_3$-Based Nanoplatelets Revealed via Magneto-Optical Spectroscopy, Nano Lett. **22**, 7011 (2022).

[38] A. Chernikov, T. C. Berkelbach, H. M. Hill, A. Rigosi, Y. Li, B. Aslan, D. R. Reichman, M. S. Hybertsen, and T. F. Heinz, Exciton Binding Energy and Nonhydrogenic Rydberg Series in Monolayer ${\mathrm{WS}}_{2}$, Phys. Rev. Lett. **113**, 076802 (2014).

[39] M. Selig, G. Berghäuser, A. Raja, P. Nagler, C. Schüller, T. F. Heinz, T. Korn, A. Chernikov, E. Malic, and A. Knorr, Excitonic linewidth and coherence lifetime in monolayer transition metal dichalcogenides, Nat Commun **7**, 13279 (2016).

[40] A. Raja, A. Chaves, J. Yu, G. Arefe, H. M. Hill, A. F. Rigosi, T. C. Berkelbach, P. Nagler, C. Schüller, T. Korn, C. Nuckolls, J. Hone, L. E. Brus, T. F. Heinz, D. R. Reichman, and A. Chernikov, Coulomb engineering of the bandgap and excitons in two-dimensional materials, Nat Commun **8**, 15251 (2017).

[41] G. H. Wannier, The Structure of Electronic Excitation Levels in Insulating Crystals, Phys. Rev. **52**, 191 (1937).

[42] A. Fetter and J. Walecka, *Quantum Theory of Many-Particle Systems* (MacGraw-Hill, New York, 1971).

[43] M. Rohlfing and S. G. Louie, Electron-hole excitations in semiconductors and insulators, Phys. Rev. Lett. **81**, 2312 (1998).

[44] M. Rohlfing and S. G. Louie, Electron-hole excitations and optical spectra from first principles, Phys. Rev. B **62**, 4927 (2000).

[45] M. Bokdam, T. Sander, A. Stroppa, S. Picozzi, D. D. Sarma, C. Franchini, and G. Kresse, Role of Polar Phonons in the Photo Excited State of Metal Halide Perovskites, Sci. Rep. **6**, 28618 (2016).

[46] M. R. Filip, J. B. Haber, and J. B. Neaton, Phonon Screening of Excitons in Semiconductors: Halide Perovskites and beyond, Phys. Rev. Lett. **127**, 067401 (2021).

[47] M. Palummo, E. Berrios, D. Varsano, and G. Giorgi, Optical Properties of Lead-Free Double Perovskites by Ab Initio Excited-State Methods, ACS Energy Lett. **5**, 457 (2020).

[48] R. I. Biega, M. R. Filip, L. Leppert, and J. B. Neaton, Chemically Localized Resonant Excitons in Silver-Pnictogen Halide Double Perovskites, J. Phys. Chem. Lett. **12**, 2057 (2021), arXiv:2102.05699.

[49] W. Meng, X. Wang, ZEWEN. XIAO, J. Wang, D. B. Mitzi, and Y. Yan, Parity-Forbidden Transitions and Their Impacts on the Optical Absorption Properties of Lead-Free Metal Halide Perovskites and Double Perovskites, J. Phys. Chem. Lett. **8**, 2999 (2017).

[50] M. Jain, P. Bhumla, M. Kumar, and S. Bhattacharya, Lead-free alloyed double perovskites: An emerging class of materials for optoelectronic applications, J. Phys. Chem. C **126**, 6753 (2022).

[51] M. Luo, Y. Zhao, A. Yang, Q. Chen, X. Zhang, and J. Luo, First-principles study on the electronic structures and optical properties of cs2xincl6 (x= ag, na), Solid State Commun. **352**, 114812 (2022).

[52] C.-J. Yu, I.-C. Ri, H.-M. Ri, J.-H. Jang, Y.-S. Kim, and U.-G. Jong, First-principles study on structural, elec-

tronic and optical properties of halide double perovskite Cs_2AgBX_6 (B = In, Sb; X = F, Cl, Br, I), RSC Adv. **13**, 16012 (2023).

[53] S. Adhikari and P. Johari, Theoretical insights into monovalent-metal-cation transmutation effects on lead-free halide double perovskites for optoelectronic applications, Phys. Rev. Mater. (2023).

[54] T. T. Tran, J. R. Panella, J. R. Chamorro, J. R. Morey, and T. M. McQueen, Designing indirect-direct bandgap transitions in double perovskites, Mater. Horiz. **4**, 688 (2017).

[55] J. A. Steele, W. Pan, C. Martin, M. Keshavarz, E. Debroye, H. Yuan, S. Banerjee, E. Fron, D. Jonckheere, C. W. Kim, W. Baekelant, G. Niu, J. Tang, J. Vanacken, M. Van der Auweraer, J. Hofkens, and M. B. Roeffaers, Photophysical Pathways in Highly Sensitive $Cs_2AgBiBr_6$ Double-Perovskite Single-Crystal X-Ray Detectors, Adv. Mater. **30**, 1 (2018).

[56] D. Bartesaghi, A. H. Slavney, M. C. Gélvez-Rueda, B. A. Connor, F. C. Grozema, H. I. Karunadasa, and T. J. Savenije, Charge Carrier Dynamics in $Cs_2AgBiBr_6$ Double Perovskite, J. Phys. Chem. C **122**, 4809 (2018).

[57] J. C. Dahl, W. T. Osowiecki, Y. Cai, J. K. Swabeck, Y. Bekenstein, M. Asta, E. M. Chan, and A. P. Alivisatos, Probing the stability and band gaps of $Cs_2AgInCl_6$ and $Cs_2AgSbCl_6$ lead-free double perovskite nanocrystals, Chem. Mater. **31**, 3134 (2019).

[58] J. D. Majher, M. B. Gray, T. A. Strom, and P. M. Woodward, $Cs_2NaBiCl_6$:Mn^2+ - A New Orange-Red Halide Double Perovskite Phosphor, Chem. Mater. **31**, 1738 (2019).

[59] A. Noculak, A. Noculak, V. Morad, V. Morad, K. M. McCall, S. Yakunin, Y. Shynkarenko, S. Yakunin, Y. Shynkarenko, M. Wörle, and M. V. Kovalenko, Bright Blue and Green Luminescence of Sb(III) in Double Perovskite Cs_2MInCl_6(M = Na, K) Matrices, Chem. Mater. **32**, 5118 (2020).

[60] M. B. Gray, S. Hariyani, T. A. Strom, J. D. Majher, J. Brgoch, and P. M. Woodward, High-efficiency blue photoluminescence in the $Cs_2NaInCl_6$: Sb^3+ double perovskite phosphor, J. Mater. Chem. C **8**, 6797 (2020).

[61] J. Deslippe, G. Samsonidze, D. A. Strubbe, M. Jain, M. L. Cohen, and S. G. Louie, BerkeleyGW: A massively parallel computer package for the calculation of the quasiparticle and optical properties of materials and nanostructures, Comp. Phys. Commun. **183**, 1269 (2012).

[62] B. A. Barker, J. Deslippe, J. Lischner, M. Jain, O. V. Yazyev, D. A. Strubbe, and S. G. Louie, Spinor GW/Bethe-Salpeter calculations in BerkeleyGW: Implementation, symmetries, benchmarking, and performance, Phys. Rev. B **106**, 115127 (2022).

[63] J. Even, L. Pedesseau, C. Katan, M. Kepenekian, J.-S. Lauret, D. Sapori, and E. Deleporte, A Solid State Physics Perspective on Hybrid Perovskite Semiconductors, J. Phys. Chem. C , 10161 (2015).

[64] M. A. Becker, R. Vaxenburg, G. Nedelcu, P. C. Sercel, A. Shabaev, M. J. Mehl, J. G. Michopoulos, S. G. Lambrakos, N. Bernstein, J. L. Lyons, T. Stöferle, R. F. Mahrt, M. V. Kovalenko, D. J. Norris, G. Rainò, and A. L. Efros, Bright triplet excitons in caesium lead halide perovskites, Nature **553**, 189 (2018).

[65] G. Biffi, Y. Cho, R. Krahne, and T. C. Berkelbach, Excitons and Their Fine Structure in Lead Halide Perovskite Nanocrystals from Atomistic GW/BSE Calculations, J. Phys. Chem. C **127**, 1891 (2023).

[66] P. Y. Yu and M. Cardona, *Fundamentals of Semiconductors* (Springer).

[67] A. Schindlmayr, Excitons with anisotropic effective mass, Euro. J. Phys. **18**, 374 (1997).

[68] G. Cappellini, R. D. Sole, and F. Bechstedt, Model dielectric function for semiconductors, Phys. Rev. B **47**, 9892 (1993).

[69] A. H. Slavney, B. A. Connor, L. Leppert, and H. I. Karunadasa, A pencil-and-paper method for elucidating halide double perovskite band structures, Chem. Sci. **10**, 11041 (2019).

[70] S. R. Kavanagh, C. N. Savory, S. M. Liga, G. Konstantatos, A. Walsh, and D. O. Scanlon, Frenkel excitons in vacancy-ordered titanium halide perovskites (Cs_2TiX_6), J. Phys. Chem. Lett. **13**, 10965 (2022).

[71] B. Cucco, C. Katan, J. Even, M. Kepenekian, and G. Volonakis, Fine structure of excitons in vacancy-ordered halide double perovskites, ACS Mater. Lett. **5**, 52 (2023).